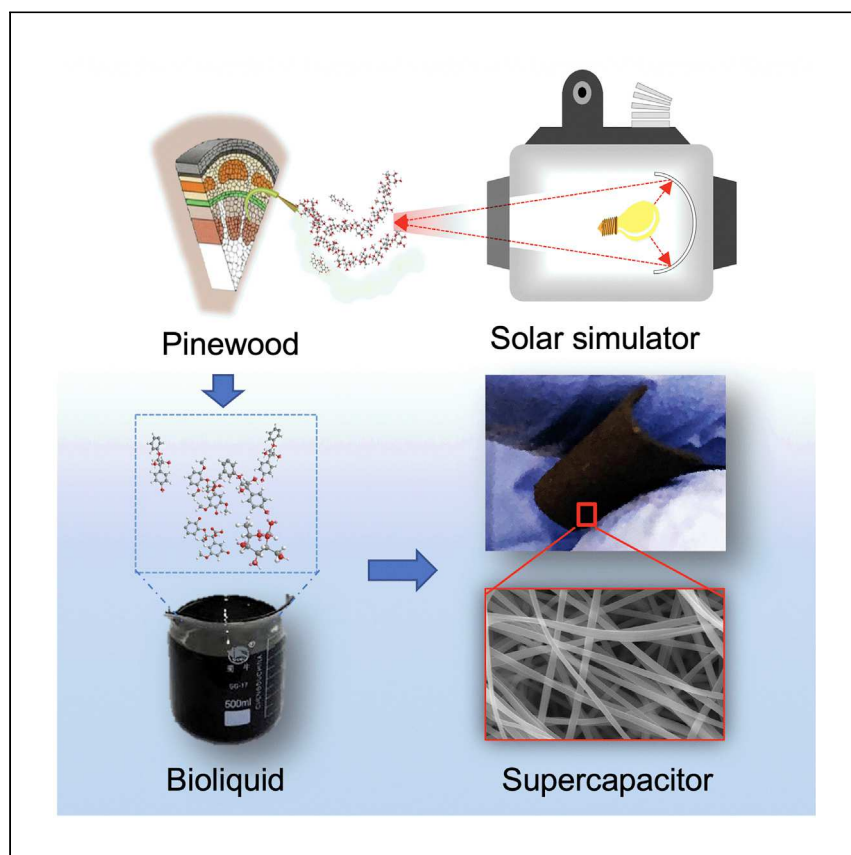


Article

Carbon Nanofibers Prepared from Solar Pyrolysis of Pinewood as Binder-free Electrodes for Flexible Supercapacitors



Tongtong Wang, Asif H. Rony, Kaidi Sun, ..., Steve J. Smith, Eric G. Eddings, Maohong Fan

mfan@uwo.edu

HIGHLIGHTS

Pinewood is pyrolyzed, generating bioliquids

These solar-derived bioliquids are rich in phenols

Binder-free electrodes prepared from bioliquids exhibit excellent flexibility

The electrochemical properties of CNF derived from these bioliquids are evaluated

The development of cost-competitive and environmentally friendly CNFs is imperative. Wang et al. report the application of solar energy for generation of bioliquid from pinewood. Carbon nanofibers derived from these bioliquids are used for the fabrication of flexible binder-free electrodes with notable electrochemical properties.

Wang et al., Cell Reports Physical Science 1, 100079

June 24, 2020 © 2020 The Author(s).

<https://doi.org/10.1016/j.xcrp.2020.100079>



Article

Carbon Nanofibers Prepared from Solar Pyrolysis of Pinewood as Binder-free Electrodes for Flexible Supercapacitors

Tongtong Wang,¹ Asif H. Rony,¹ Kaidi Sun,¹ Weibo Gong,¹ Xin He,¹ Wenyang Lu,¹ Mingchen Tang,¹ Runping Ye,¹ Jiuling Yu,² Lin Kang,³ Hongmei Luo,² Steve J. Smith,³ Eric G. Eddings,⁴ and Maohong Fan^{1,5,6,7,*}

SUMMARY

Solar pyrolysis of renewable biomass has huge potential for sustainable production of fuel or chemical feedstock for the activated carbon materials. Here, we report a method for producing high-quality carbon nanofiber (CNF) precursor and subsequently CNFs as a low-cost and eco-friendly energy storage material. Specifically, pinewood is pyrolyzed with solar energy to generate a phenol-rich bioliquid precursor that is found to be a strong candidate for synthesizing binder-free flexible electrode materials via electrospinning. The CNFs prepared with 30% solar-driven bioliquids and 70% polyacrylonitrile have a high specific surface area and rich microstructure, which are the key to its electrochemical performance in terms of specific capacitance (349 F g^{-1} at the current density of 0.5 A g^{-1}) with notable rate performance, reversibility, and cycling stability in 6 M KOH aqueous electrolyte. Thus, solar bioliquids are feasible CNF precursors, and such derived CNFs have potential to be applied in energy storage devices.

INTRODUCTION

The development and utilization of green and renewable energies, such as solar energy,¹ wind energy,² and geothermal energy,³ have been increasing to partly replace fossil energy. Therefore, energy storage devices, such as supercapacitors, batteries, or hybrid systems, are in high demand.⁴ Among them, supercapacitors attract much attention as an energy reservoir or a power buffer due to their high power density, fast charging ability, superior low-temperature performance, and long cycle life. Compared with lithium-ion batteries, supercapacitors exhibit lower energy density, limiting their applications as primary power devices.^{5–9} Thus, supercapacitor electrodes made of porous and nanotextured carbon-based materials are gaining more and more interest, owing to their competitive properties, including high specific area, high conductivity, formation of porous network structures, and physicochemical stability.^{10,11}

Nanostructured carbon materials, including activated carbons (ACs),^{12–14} carbon black,^{15–17} carbon nanotubes (CNTs),^{10,11} graphene,^{18,19} and carbon nanofibers (CNFs), have been studied to meet the demand in high energy density supercapacitor electrodes. ACs have a small specific capacitance $<200 \text{ F g}^{-1}$, even with a fairly high specific surface area of $1,000\text{--}3,000 \text{ m}^2 \text{ g}^{-1}$.²⁰ CNTs have unique pore structures with excellent electrical and mechanical properties, but their specific

¹College of Engineering and Applied Sciences, University of Wyoming, Laramie, WY 82071, USA

²College of Engineering, New Mexico State University, Las Cruces, NM 88003, USA

³Nanoscience and Nanoengineering Ph.D. Program, South Dakota School of Mines and Technology, Rapid City, SD 57701, USA

⁴College of Engineering, University of Utah, Salt Lake City, UT 84112, USA

⁵School of Civil and Environmental Engineering, Georgia Institute of Technology, Atlanta, GA 30332, USA

⁶School of Energy Resources, University of Wyoming, Laramie, WY 82071, USA

⁷Lead Contact

*Correspondence: mfan@uwyo.edu
<https://doi.org/10.1016/j.xcrp.2020.100079>



capacitance $<100 \text{ F g}^{-1}$ is limited by the small specific surface area of $120\text{--}500 \text{ m}^2 \text{ g}^{-1}$.^{21,22} The specific capacitance of graphene is restricted by the exfoliation approach.²³ The investigation of supercapacitors prepared with chemical vapor deposition (CVD)-based CNFs began in 2006 using materials fabricated from ethanol over Fe-Ni alloy catalyst.²² CVD-derived supercapacitors are low in specific capacitance of $10\text{--}50 \text{ F g}^{-1}$ due to their small specific surface area ($10\text{--}50 \text{ m}^2 \text{ g}^{-1}$).²⁴ However, the aforementioned supercapacitors are not flexible, which is a critical characteristic for wearable devices.²⁵ Electrospun CNFs can overcome these disadvantages due to their self-supporting characteristics, which allow the preparation of high-conductivity binder-free electrodes without the need for insulating adhesives, such as polyvinylidene fluoride and polytetrafluoroethylene.^{19,26,27} The majority of precursors for electrospun CNFs are prepared from synthetic organic reagents,^{28,29} leading to not only high cost but also potential environmental pollution issues. Hazardous HCN is released during the stabilization and carbonization processes.^{30–33} Hence, the development of cost-competitive and environmentally friendly CNFs synthesized precursors is desirable.

At the same time, inexpensive renewable biomass materials, such as sawdust, rice husk, and corn stover, are available in large quantities as waste from forestry and agriculture. These have been considered as promising candidates for CNFs precursors.¹¹ The conventional method of conversion to bioliquids is thermal pyrolysis, requiring electricity as a heat source.^{34,35} This conversion process is not necessarily environmentally friendly. A renewable alternative would be to exploit heat from concentrated solar energy,³⁶ a sustainable, clean, renewable energy source. The solar pyrolysis of biomass was researched and analyzed.³⁷ However, the application of solar-pyrolysis-derived bioliquids from biomass in energy storage has not been reported in the literature to the best of our knowledge.

Pinewood is a promising bio-renewable resource for producing CNFs precursors because bioliquid derived from pinewood contains a high concentration of the aromatic compounds desired for CNFs precursor synthesis.³⁸ Also, the CNFs derived from the bioliquids differ in quality to those produced with state-of-the-art thermal and solar pyrolysis processes.³⁷ The prepared CNFs composed of 70% solar-driven bioliquids and 30% polyacrylonitrile (PAN) have a high specific surface area of $747.8 \text{ m}^2 \text{ g}^{-1}$. They show a superior specific capacitance of 349 F g^{-1} with notable rate performance, reversibility, and cycling stability in 6 M KOH aqueous electrolyte.

RESULTS AND DISCUSSION

Properties of Bioliquids

The thermogravimetric analyzer (TGA) and derivative thermogravimetric (DTG) profiles in [Figure 1A](#) demonstrate the individual devolatilization behaviors of pinewood particles and dewatered solar-derived bioliquid (DWSDBL) and dewatered thermal-derived bioliquid (DWTDBL). The TGA curves of DWSDBL and DWTDBL show similar trends, which involve a feature of a single reaction stage embodied as an apparent DTG peak during the thermal decomposition process, resulting in the fixed carbon yields of 6.16 wt % and 17.47 wt %, respectively. Particularly, the weight loss of DWTDBL is faster than DWSDBL, as shown in [Figure 1A](#). The boiling temperature range of DWSDBL is higher than that of DWTDBL. The temperatures of DTG curve peaks of DWSDBL and DWTDBL are 85.2°C and 244.6°C , respectively. Both TGA and DTG curves show that there are considerable amounts of light compounds in both bioliquids. The average molecule weight of DWSDBL is higher than that of DWTDBL. Also, molecules released at low temperatures are not useful to CNFs synthesis.

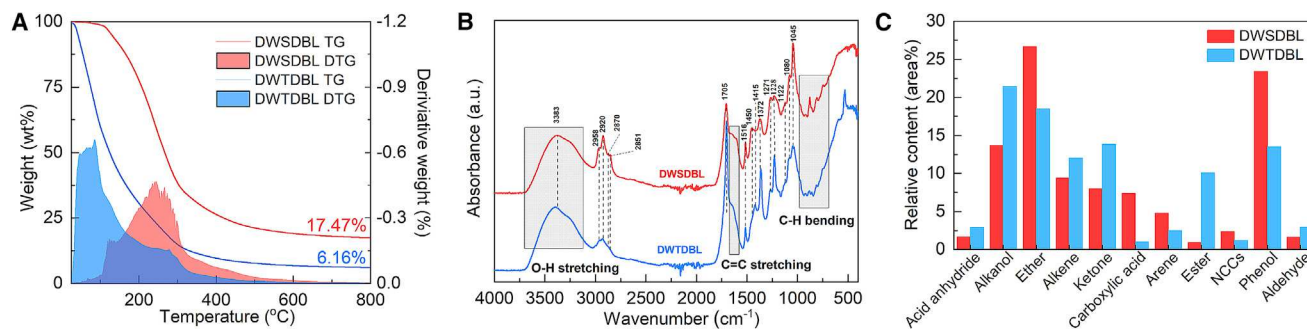


Figure 1. Comparison of Thermogravimetric and Structural Characteristics of DWSDBL and DWTDBL

(A–C) (A) Thermogravimetric analysis (TG) and its negative first derivative thermogravimetric (DTG) curves, (B) FTIR spectra, and (C) distribution of compounds with different functional groups identified with GC-MS.

Fourier transform infrared (FTIR) analyses were performed on DWSDBL and DWTDBL to study their different organic species and functional groups shown in Figure 1B and Table S1. The abundant phenolic and alcoholic hydroxyl groups in DWSDBL and DWTDBL are proved by the broad absorption bands for O–H stretching at the range of 3000–3600 cm^{-1} . The conclusion is confirmed by the peaks of 1,704, 1,122, and 1,080 cm^{-1} (C–O stretching of alcohol and phenol).^{41,42} Typically, the strong and sharp peaks of 1,704 and 1,415 cm^{-1} in DWTDBL illustrates it is rich of alcohol-containing compounds.⁴³ The strong peaks around 2,958, 2,925, 2,870, 2,851, and 1,450 cm^{-1} assigned to alkane C–H stretching vibration suggest the aliphatic moieties are generated in the DWSDBL and DWTDBL. The anhydride CO–O–CO stretching vibration band at 1,045 cm^{-1} and N–O stretching vibration at 1,516 cm^{-1} mean the aldehyde and nitro compounds are generated in DWSDBL and DWTDBL.⁴⁴ The intensity of peak at 1704 cm^{-1} for conjugated aldehyde C=O stretching vibration is higher in DWTDBL than that in DWSDBL, which means ketone, ester, and acid anhydride compounds are abundant in DWTDBL. The intensive peak of 1,271 cm^{-1} belonging to ring vibration of aromatic highlights the abundant aromatic content in DWSDBL. Besides, the stronger signal of C–O stretching vibration related to 1,228 cm^{-1} is detected in the DWTDBL.^{45–47} It is seen that aromatic C=C bonds (1,678–1,600 cm^{-1}) and C–H bending vibration absorption bands (880–730 cm^{-1}) are present in the DWSDBL and demonstrate that aromatic structures are rich in the bioliquids. Based on the above analysis, solar and thermal pyrolysis are a process of degradation of pinewood particles (PPs) and the derived DWSDBL and DWTDBL are affluent in the oxygen-containing functional compounds in the formation of the carbon-oxygen bond (C–O) in ether, ester, and hydroxyl group (C–OH) in alkanol and phenol, which could enhance the energy storage performance in electrochemical supercapacitors and electrolyte wettability.^{48,49}

Gas chromatography-mass spectrometry (GC-MS) was used for further investigating the composition differences of DWSDBL and DWTDBL resulting from solar and thermal pyrolysis, and the results are shown in Figures 1C and S1. The compounds and their molecular formula, masses, and relative concentrations in both DWSDBL and DWTDBL are listed in Tables S2 and S3. Both bioliquids contain acid anhydride, alkanol, ether, alkene, ketone, carboxylic acid, arene, ester, phenol, aldehyde, and N-containing compounds (NCCs), although alkanol, ether, and ketone as well as phenol dominate. The GC-MS results indicate that the reactions in both DWSDBL and DWTDBL production processes are quite complex. However, the differences between the two bioliquids are obvious. First, DWSDBL contains much higher concentrations of aromatic compounds, showing peaks mainly at 12.263, 19.293, and

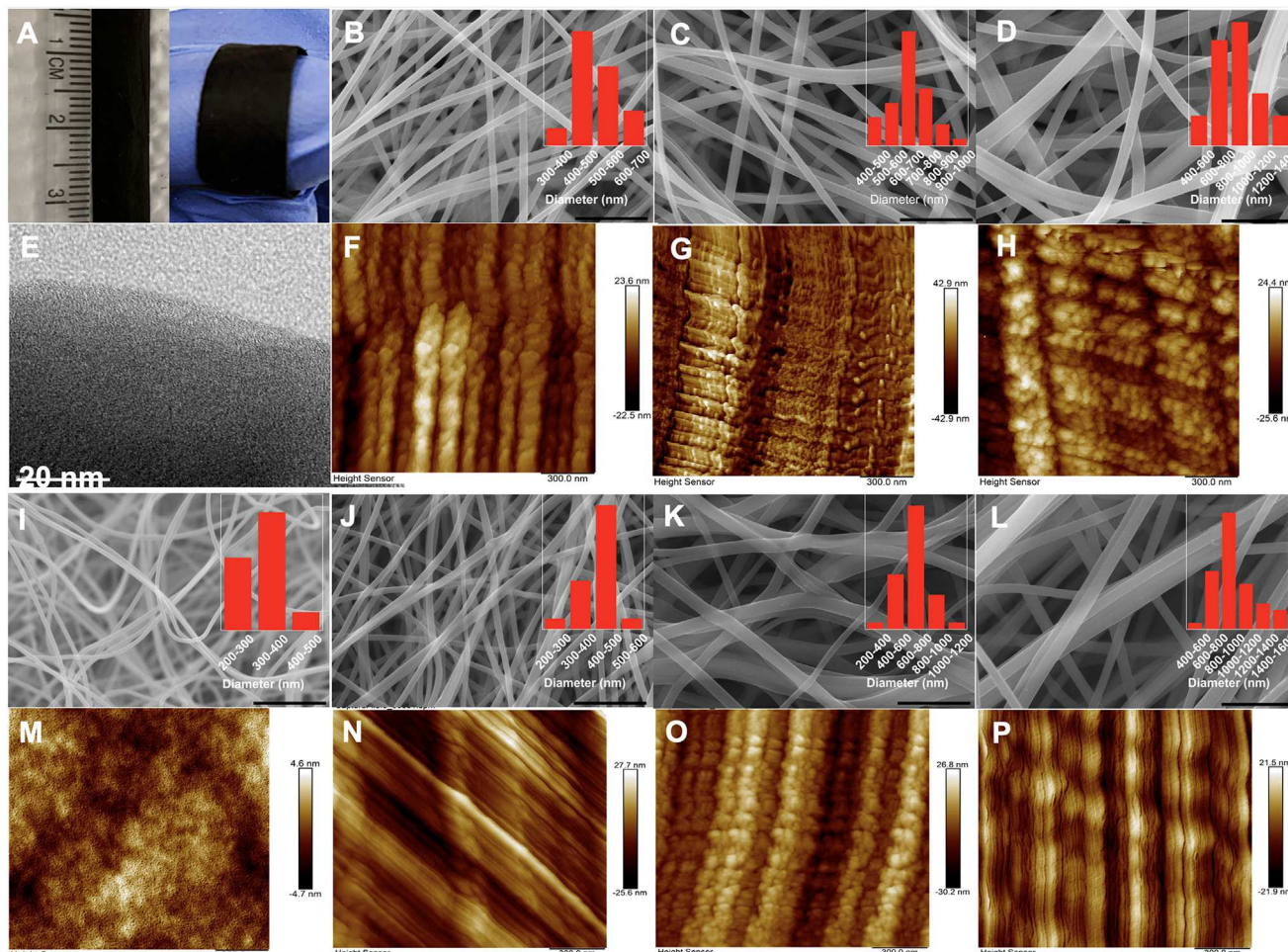


Figure 2. Morphology Difference of PAN- and Bioliquids-based Supercapacitor Electrodes
(A–P) (A) Photograph and (E) TEM image of prepared DWSDBL30PAN70 CNF, SEM, and AFM images of CNFs (B and F) DWSDBL10PAN90, (C and G) DWSDBL30PAN70, (D and H) DWSDBL50PAN50, (I and M) PAN, (J and N) DWTDBL10PAN90, (K and O) DWTDBL30PAN70, and (L and P) DWTDBL50PAN50. Inset of SEM images: corresponding fibers diameter distribution is shown; the scale bar of SEM is 5 μm . The scale bar of AFM is 300 nm.

38.946 min, including those of phenols at 12.263 and 19.293 min. Aromatic compounds in DWSDBL account for $\sim 28\%$ among those with relative areas being more than or equal to 3%, and 81.5% of the aromatic compounds are phenols. Moreover, the relative areas of non-aromatic compounds, including ester, alkyne, ketone, and aldehyde in DWTDBL, are up to 84%. The major characteristic peaks of ester, alkyne, ketone, and aldehyde in DWTDBL are at 3.061, 9.254, 12.538, and 22.457 min. The results measured with GC-MS are in agreement with those obtained from FTIR observations.

Characteristics of Bioliquid-based Supercapacitor Electrodes

The morphologies and structures of fabricated CNFs based on PAN after two thermal treatments, stabilization, and carbonization were characterized using scanning electron microscopy (SEM), transmission electron microscopy (TEM), and atomic force microscopy (AFM) in Figures 2 and S2. According to the SEM images in Figure 2, continuous and smooth CNFs without the presence of any bead defects were prepared with the bioliquids-PAN mixtures containing 10 wt %, 30 wt %, and

50 wt % bioliquids, respectively. Thus, adding the proper amounts of bioliquids to PAN does not affect the physical continuity of CNFs. The diameters of PAN, DWSDBL10PAN90, DWSDBL30PAN70, and DWTDBL10PAN90 CNFs are 330 nm, 500 nm, 650 nm, and 420 nm, respectively. The introduction of bioliquids increased the diameters of CNFs, which is not beneficial to the increase in the capacities of CNFs. In other words, bioliquids and PAN mixtures can be used for successfully preparing CNFs with conjugated ladder structure⁵⁰ via peroxidation, cyclization, aromatization, and cross-linking reactions. The CNFs are randomly distributed and cross-linked with each other. However, they are not intimately interconnected, which could impede electrical conductivity reflected in the electrochemical impedance spectroscopy (EIS) tests. The CNFs of DWSDBL50PAN50, DWTDBL30PAN70, and DWTDBL50PAN50 CNFs show obviously fuse and melt together, and their diameter increased to 950 nm, 670 nm, and 1,010 nm, respectively. This resulted in the restricted movement among CNFs, which is problematic when they are used as flexible energy storage materials due to their brittle properties. Compared to the SEM images of the bioliquids-PAN-mixtures-based CNFs, those PAN-based CNFs show smaller diameters.

The surface of PAN CNF presents a poor depth of field, +4.6 to -4.7 nm, based on the observation with AFM shown in Figure 2M. Apparently, bioliquids-PAN-mixtures-based CNFs have more pores and rougher surfaces of fields with various depths, resulting from the evolutions of light components as the gases from the nanofiber surface during the stabilization and carbonization processes. DWSDBL30PAN70 CNF shows the deepest surface from +42.9 to -42.9 nm in Figure 2C, indicating its high specific surface areas required for the high special capacitance as a supercapacitor electrode. Besides, the TEM image of DWSDBL30PAN70 CNF shows the turbostratic carbonaceous structures and haphazardly folded carbon sheets ascribed to the amorphous CNF prepared under carbonization temperature of 800°C.⁵¹

X-ray diffraction (XRD) patterns in Figure 3A show two broad diffraction peaks centered at 2θ angles of 25° and 43°, belonging to (002) and (100) reflections of graphitic carbon, respectively, attributed to the destructions of PAN and bioliquid structures during carbonization or graphite formation processes.^{51,52} The characteristic diffraction peak of PAN-based CNFs appears at $\sim 25.16^\circ$ ascribed to (002) crystallographic plane of graphite crystallites, although those of DWSDBL10PAN90, DWSDBL30PAN70, DWSDBL50PAN50, DWTDBL10PAN90, DWTDBL30PAN70, and DWTDBL50PAN50 CNFs show at 24.49°, 24.46°, 24.44°, 24.98°, 24.76°, and 24.60°, respectively, indicating that the addition of bioliquids can enlarge the interlayer spacing in the CNFs for their complex and oxygen-containing functional compounds. Furthermore, the interlayer spacings of CNFs obtained from DWSDBL-PAN are smaller than those from DWTDBL-PAN due to the higher aromatic degrees of DWSDBL.

The Raman spectra in Figure 3B of the CNFs commonly show as a broadband peak at $1,582\text{ cm}^{-1}$ (G band) relative to the ordered graphitic crystallites and another band at $1,360\text{ cm}^{-1}$ (D band) relative to the disordered carbon structures. The intensity ratio (R value) of D band to G band (I_D/I_G) determines the degree of crystallization and defect in carbon materials.⁵³ PAN-based CNF shows the lowest R value of 1.007 due to its uniform molecular structure. The R values of DWSDBL10PAN90, DWSDBL30PAN70, DWSDBL50PAN50, DWTDBL10PAN90, DWTDBL30PAN70, and DWTDBL50PAN50 CNFs are 1.015, 1.027, 1.040, 1.045, 1.049, and 1.052, respectively. The R values of bioliquids-PAN-mixtures-based CNFs are higher than

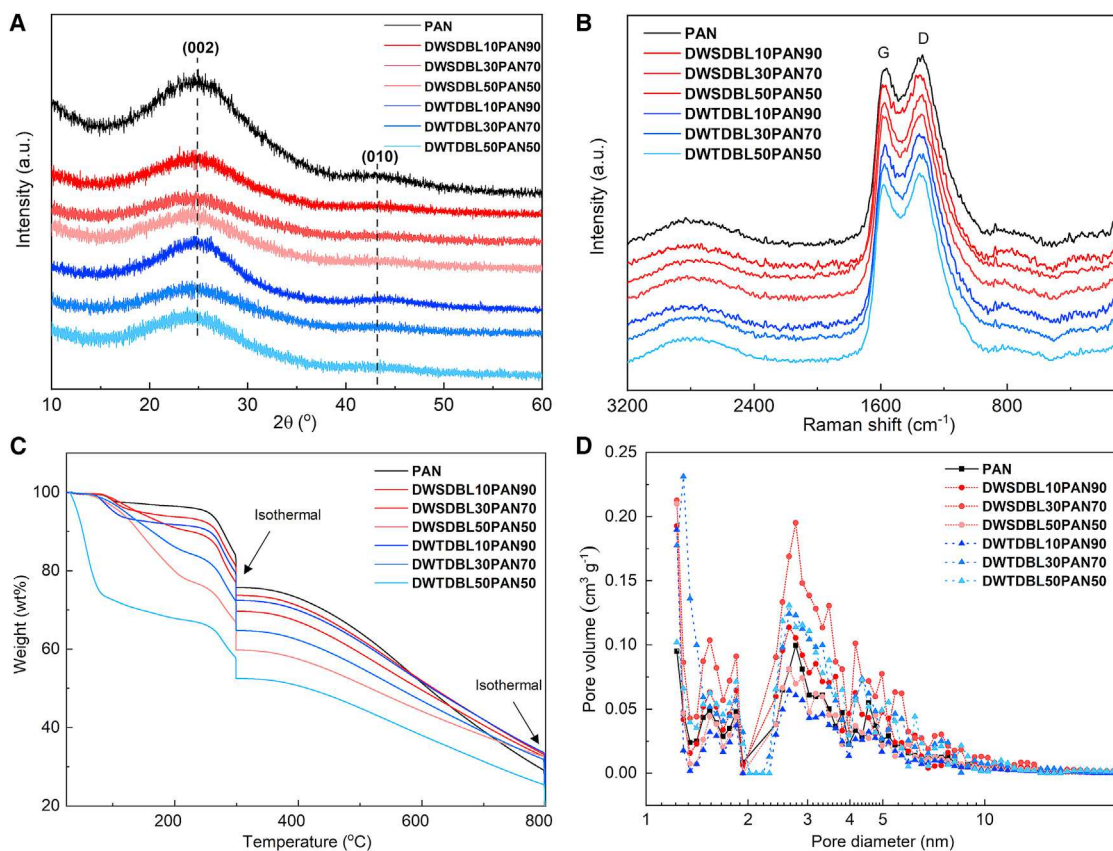


Figure 3. Characterization of PAN- and Bioliquid-based Supercapacitor Electrodes

(A–D) (A) XRD profiles, (B) Raman spectra, (C) TGA curves, and (D) the pore size distribution curves using the NLDFT method of PAN, DWSDBL10PAN90, DWSDBL30PAN70, DWSDBL50PAN50, DWTDBL10PAN90, DWTDBL30PAN70, and DWTDBL50PAN50 CNFs. TGA profile: stabilization: 300°C for 3 h (1°C min⁻¹ ramp rate); carbonization: 270°C–800°C (5°C min⁻¹ ramp rate).

those of PAN-based CNFs and increase with the quantities of introduced bioliquids in PAN. The structure changes of CNFs and the formation of defects result from the increase in functional groups of bioliquids. The introduced residual oxygen and other heteroatoms in CNFs distort the ordered sp² bonding carbon atoms (relative to G-band) into disordered sp³ tetrahedral hybridized state (relative to D-band). Moreover, the more porous structures of bioliquid-mixture-based CNFs led to more disorders and defects, which is consistent with the observations with AFM and Brunauer-Emmett-Teller (BET). Obviously, compared with CNFs derived from DWTDBL, the DWSDBL-based CNFs have lower R values and better graphite structures due to high concentrations of arene compounds. The fact reveals the advantage of solar pyrolysis for producing bioliquids and the subsequent CNFs.

The thermal characteristics of the as-spun nanofibers with TGA analysis are shown in Figures 3C and S3. The rate of weight loss of as-spun nanofibers decreases with temperature due to the releases of small gaseous molecules during the oxidation process. The yields of PAN, DWSDBL10PAN90, DWSDBL30PAN70, DWSDBL50PAN50, DWTDBL10PAN90, DWTDBL30PAN70, and DWTDBL50PAN50 CNFs after stabilization stage are 75.76%, 73.75%, 69.67%, 59.78%, 72.74%, 64.77%, and 52.53%, respectively. The TGA data show that the structure of PAN is more stable than those of bioliquids. The weight-loss rates of as-spun PAN-DWTDBL nanofibers are significantly higher than those of as-spun DWSDBL-PAN nanofibers because the DWTDBL

Table 1. Structural Characteristics of CNFs

Sample	S_{BET} ($\text{m}^2 \text{g}^{-1}$)	S_{DFT} ($\text{m}^2 \text{g}^{-1}$)	V_t ($\text{cm}^3 \text{g}^{-1}$)	Pore Volume in $\text{cm}^3 \text{g}^{-1}$ and Pore vol %	
				$V_{<2 \text{ nm}}$	$V_{>2 \text{ nm}}$
PAN	343.7	288.0	0.306	0.089 (29.1%)	0.217 (70.9%)
DWSDBL10PAN90	549.4	505.7	0.445	0.168 (37.8%)	0.277 (62.2%)
DWSDBL30PAN70	747.8	629.7	0.645	0.195 (30.2%)	0.450 (69.8%)
DWSDBL50PAN50	490.5	485.4	0.366	0.170 (46.4%)	0.196 (53.6%)
DWTDBL10PAN90	427.0	427.9	0.306	0.152 (49.7%)	0.154 (50.3%)
DWTDBL30PAN70	580.7	470.2	0.476	0.157 (33.0%)	0.319 (67.0%)
DWTDBL50PAN50	450.9	358.4	0.421	0.103 (24.5%)	0.318 (75.5%)

Pore size distribution and volume are calculated using the NLDFT method. S_{BET} represents specific surface area by BET method; S_{DFT} is specific surface area calculated by DFT method; V_t denotes total pore volume of the pores; $V_{<2 \text{ nm}}$ is total pore volume of the pores with their diameter less than 2 nm; and $V_{>2 \text{ nm}}$ is total pore volume of the pores with their diameter larger than 2 nm.

contains more light molecules. The yields of established PAN, DWSDBL10PAN90, DWSDBL30PAN70, DWSDBL50PAN50, DWTDBL10PAN90, DWTDBL30PAN70, and DWTDBL50PAN50 CNFs after temperature ramping from 300°C to 800°C at 10°C min⁻¹ and carbonization at 800°C for 1 h are 18.11%, 24.14%, 25.44%, 27.34%, 23.95%, 25.21%, and 26.10%, respectively. The stabilized PAN-based nanofiber shows the highest weight loss, although stabilized DWSDBL50PAN50 nanofiber has the lowest loss due to its highest percentage of aromatic compounds.

The specific surface areas of supercapacitor electrodes, mainly determined by the characteristics of micropores, are critical to their energy storage capacities.⁵⁴ The non-localized density functional theory (NLDFT) method was used to determine pore size distribution.^{55,56} The specific surface areas and pore sizes are plotted in Figures 3D and S4, and other parameters of the supercapacitor electrodes are summarized in Table 1. All the CNF samples show VI type adsorption isotherm, indicating the coexistence of micropores, mesopores, and macropores in the materials. The PAN-based CNFs exhibit the lowest specific surface area (343.7 m² g⁻¹) and pore volume (0.306 cm³ g⁻¹), although DWSDBL30PAN70 possesses the highest specific surface area (747.8 m² g⁻¹) and pore volume (0.645 cm³ g⁻¹). The specific surface area or S_{BET} (580.7 m² g⁻¹) and pore volume or V_t (0.476 cm³ g⁻¹) of DWTDBL30PAN70 CNFs are between those of PAN-based CNFs and DWSDBL30PAN70 CNFs. According to the literature,⁵⁴ the higher the specific surface area is, the higher the specific capacitance is. Thus, the specific capacitances (Cs) of the just-mentioned materials should be in the order of DWSDBL30PAN70 > DWTDBL30PAN70 > PAN-based CNFs. Also, the S_{DFT} and $V_{<2 \text{ nm}}$ as well as $V_{>2 \text{ nm}}$ values of those three materials follow the same order. It should be mentioned that the $V_{>2 \text{ nm}}$ value of the DWSDBL50PAN50 CNF is the lowest, resulting from the fusing of its CNFs, which can be observed from its SEM image.

X-ray photoelectron spectroscopy (XPS) tests were used to further investigate the detailed elemental compositions and bonding configurations of the prepared CNFs. The results are shown in Figure 4 and Table S4. The three typical peaks of C and N as well as O of all the CNFs are located at 284.8, 401.0, and 532.6 eV, respectively. The PAN-based CNF shows the lowest C contents of 83.9% and the highest N content of 12.9%, due to its N-rich precursor. The C contents in bioliquid-PAN-mixtures-based CNFs increase with the quantities of the introduced bioliquid in DWSDBL10PAN90, DWSDBL30PAN70, DWSDBL50PAN50,

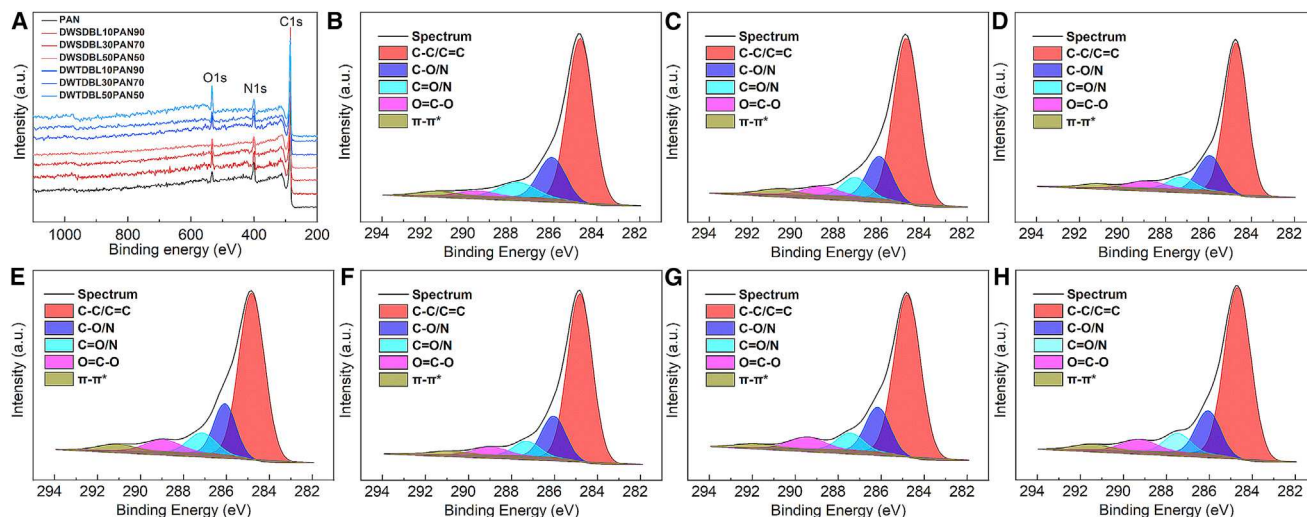


Figure 4. XPS Analysis of the Fabricated Supercapacitor Electrodes

(A–H) (A) XPS survey and high-resolution C1s spectra of (B) DWSDBL10PAN90, (C) DWSDBL30PAN70, (D) DWSDBL50PAN50, (E) PAN, (F) DWTDBL10PAN90, (G) DWTDBL30PAN70, and (H) DWTDBL50PAN50 CNFs.

DWTDBL10PAN90, DWTDBL30PAN70, and DWTDBL50PAN50 CNFs, corresponding to 85.2%, 87.1%, 92.2%, 86.6%, 87.4%, and 88.5%, respectively, an indication of their richness in aromatic groups in bioliquids-PAN mixtures that are more stable during the thermal treatment process. N contentions start to decrease with quantities of the PAN added to the bioliquid-PAN mixture. The high-resolution spectra of C1s were collected to further investigate the oxygen-associated functional groups that could promote the electrochemical performance of the CNFs.^{57–59} The five peaks located at 284.8 eV, 286.0 eV, 287.3 eV, 288.9 eV, and 290.9 eV should be assigned to C–C/C=C, C–O/N, C=O/N, O=C–O, and π - π^* respectively.^{60–62} The contents of C–C/C=C and π - π^* in bioliquids-PAN composite CNFs increase with the amounts of the added bioliquids. Typically, the contents of π - π^* in DWSDBL-PAN-mixtures-based CNFs are higher than those of DWTDBL-PAN-mixtures-based CNFs for their rich aromatic structures, which is beneficial to the improvement of their conductivities.¹¹ The C–O/N, C=O/N, and O=C–O groups on the surfaces of bioliquids-PAN-mixtures-based CNFs could enhance the pseudofaradaic behaviors and wettability and thus hydrophilic properties.⁶³ The introduction of O from bioliquids into CNFs could promote the Faradaic reactions at the interface of the electrolyte/electrode interface and improve their energy storage abilities.^{59,64,65}

The cyclic voltammetry (CV), galvanostatic charge-discharge (GCD), and EIS were collected for comparing the electrochemical performances of the supercapacitor electrodes, and the results are presented in Figure 5. All the curves of bioliquids-PAN-composite-based CNFs with symmetric rectangular-like shapes commonly show one pair of broad Faradaic peaks, typically appearing in an S-shaped CV curve at anodic scale, which is a CV character of the oxygen-containing group in carbon material in alkaline solution. The electrochemical double-layer capacitances (EDLCs) are mainly determined by specific surface area, although the pseudocapacitive effect results from the reversible reduction/oxidation of C–O/N, C=O/N, and O=C–O in DWSDBL30PAN70 CNF. The oxygen-containing functional groups, like carboxyl and phenol groups, react with hydroxyl ions (OH^-) in 6 M KOH aqueous electrolyte depicted in Equations 1 and 2.⁵⁷ Bioliquids-based CNFs have larger CV areas than PAN-based CNFs. Therefore, the introduction of bioliquids leads to

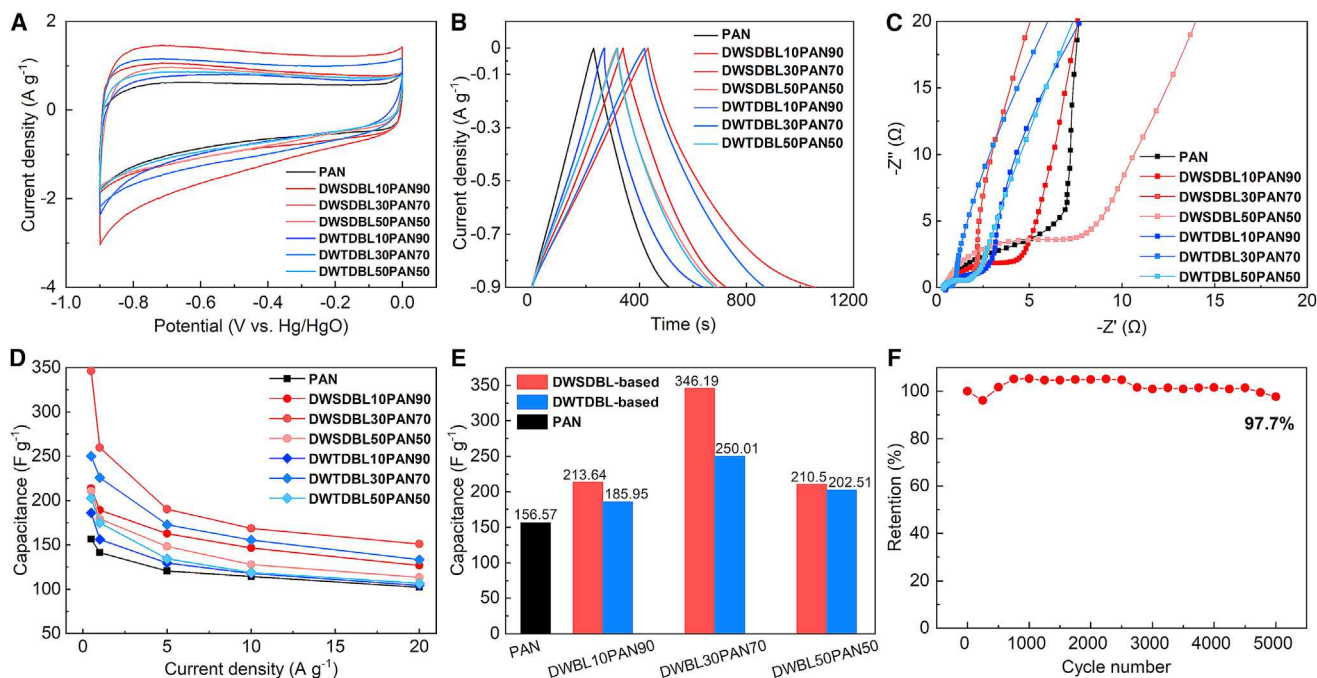
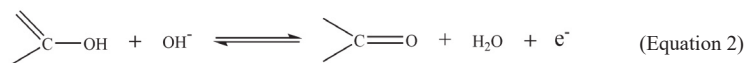
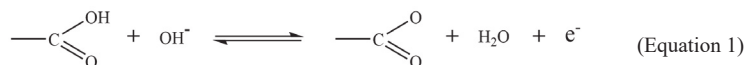


Figure 5. Electrochemical Performances of CNFs Measured in a Three-Electrode System

(A–F) (A) CV profiles at scan rates of 5 mV s^{-1} , (B) galvanostatic charge-discharge profiles at the current density of 0.5 A g^{-1} , (C) EIS spectra from 100 kHz to 0.01 Hz, (D) specific capacitance versus current density, (E) specific capacitance at the current density of 0.5 A g^{-1} , and (F) the cycling performance of DWSDL30PAN70 CNF at the current density of 10 A g^{-1} .

an increase in capacitance. The similarity in the S sections of the CV curves in Figure 5A reveals all DWSDL30PAN70-composite-based CNFs contain similar oxygen/nitrogen-containing functional groups.



In Figure 5B, the GCD plots of all CNF supercapacitor electrodes show the quasi-triangular shape at the current density of 0.5 A g^{-1} . The calculated specific capacitance of the PAN-based CNF shows the lowest value, 156.57 F g^{-1} , which is consistent with that in literature.⁶⁶ Those of bioliquids-PAN-mixture-based CNFs are significantly higher than that of PAN-based CNF. The calculated specific capacitances of DWSDL10PAN90, DWSDL30PAN70, DWSDL50PAN50, DWTDBL10PAN9, DWTDBL30PAN70, and DWTDBL50PAN50 CNFs are 213.64, 346.19, 210.5, 185.95, 250.01, and 202.51 F g^{-1} , respectively. The changing trend of specific capacitances of bioliquids-PAN mixture CNFs is in accordance with those of the specific surface areas and micropores volume confirmed by BET in Table 1. Thus, the DWSDL30PAN70 CNF shows the highest specific capacitance, 121% and 38.5% increases compared to those of PAN-based CNF and DWTDBL30PAN70 CNF, respectively. The results indicate that surface functional groups contribute to the pseudocapacitance, although specific surface area plays a more important role in increasing specific capacitance of bioliquids-PAN-mixture-based CNFs via

the suitable light compounds in DWSDLs and their impacts during the subsequent preparation of CNFs.

Each Nyquist plot of all seven CNFs in Figure 5C used for studying the electron/ion transport process of prepared CNFs as electrodes has a typical small semicircle in the high-frequency region and a straight line at low frequency.^{55,67} Also, the Nyquist impedance plots were fitted and results are shown in Figure S5 and Table S5.⁶⁸ The cell resistances correspond to the intercept of the semicircle on the real axis at the frequency of 10 kHz. The PAN-based CNF has the highest resistance (0.495 Ω) with the lowest relative π - π^* bonds. The resistances of DWSDL10PAN90, DWSDL30PAN70, DWSDL50PAN50, DWTDBL10PAN90, DWTDBL30PAN70, and DWTDBL50PAN50 CNFs are 0.431, 0.390, 0.361, 0.459, 0.385, and 0.376 Ω , respectively. The resistance change trend is in line with that of the relative π - π^* bonds. Based on the diameters of the semicircles on the real axis in the high-frequency range, the bioliquids-PAN CNFs show the smallest diameter representing the resistances or the electron transport at the interface of the collector/CNFs during the charge and discharge process, resulting from the lowest concentration of oxygen-containing functional compounds on the surface. The slopes of straight lines at the low-frequency region reflect the diffusion resistance or the degree of difficulty in entering of electrons into the pores on CNFs. The slopes of PAN-based CNF are almost vertical. The slopes of DWSDL-PAN-mixtures-based CNFs are lower than those of DWTDBL-PAN-mixtures-based CNFs, indicating the high concentrations of oxygen-containing functional groups in DWSDL, which can increase the ionic diffusion impedance in the pores of the CNFs.⁵⁹

The three-electrode CV and GCD curves of DWSDL30PAN70 CNF in 6 M KOH electrolyte at different scan rates and current density are shown in Figure 5F. The DWSDL30PAN70 CNF demonstrates the excellent cycling stability with 97.7% retention after 5,000 cycles at a current density of 10 A g⁻¹. It is worth noting that the specific capacitance increases by 5% after 1,000 cycles, which resulted from the activation process that allows the trapped ions to gradually diffuse out.^{59,69} A two-electrode symmetrical capacitor device was also assembled using two DWSDL30PAN70 CNF samples with the same sizes and weight to further investigate its electrochemical performances in 6 M KOH electrolyte, and the results are given in Figure 6. The CV profiles retain the rectangular-like shape, even at a high scan rate of 100 mV s⁻¹, and GVD profiles exhibit a quasi-triangular shape at different current densities, showing its remarkable rate performance and reversibility. The electrochemical performance of the DWSDL30PAN70 CNF was evaluated using the Ragone plot shown in Figure 6C. Its maximal energy density (5.11 Wh kg⁻¹) and power density (5,000 W kg⁻¹) are comparable to the highest values recently reported,^{66,70,71} which is significantly higher than those of commercial carbon-based supercapacitors.⁷² Moreover, the capacitance retention after 5,000 cycles at a current density of 10 A g⁻¹ is 99.3%, which is also comparable to the best performance in literature.^{65,71,73} The capacitance retention after the first 3,000 cycles is higher than 100%, which can be attributed to the increase in the active sites due to the gradual infiltration of electrolytes during the charging and discharging process.^{65,69} The comparison between this work and those reported in the literature is summarized in Table S6.

In summary, solar pyrolysis is a promising method for producing flexible CNF precursors from biomass. It was used for processing pinewood particles, and the obtained bioliquid was successfully used for fabricating superior-capacity CNF synthesized via bioliquid electrospinning, stabilization, and carbonization. The structure

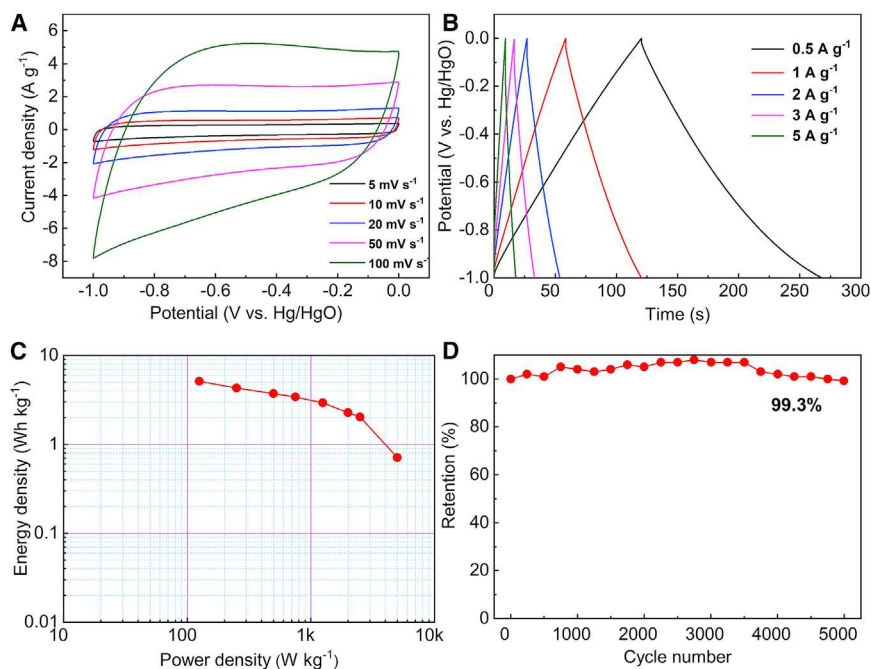


Figure 6. Electrochemical Performances of DWSDBL30PAN70 CNF Measured in a Two-Electrode System

(A–D) (A) CV profiles at scan rates from 5 to 100 mV s⁻¹, (B) galvanostatic charge-discharge profiles at the current density from 0.5 to 5 A g⁻¹, (C) Ragone plots, and (D) cyclic performance at 10 A g⁻¹.

characteristics of the obtained DWSDBL, including appropriate light fractions and oxygen-rich compounds, including phenols, ethers, ketone, and ester, are desirable for preparing high micropores and thus high specific area, which lead to the high performance of the CNFs in terms of specific capacitance, capacitance retention, and power and energy densities.

EXPERIMENTAL PROCEDURES

Resource Availability

Lead Contact

Further information and requests for resources and reagents should be directed to and will be fulfilled by the lead contact, Prof. Dr. Maohong Fan (mfan@uwyo.edu).

Materials Availability

This study did not generate new unique reagents.

Data and Code Availability

All data associated with the study are included in the paper and the supplemental information. Additional information is available from the Lead Contact upon reasonable request.

Materials

Pinewood was collected from beetle-killed pine trees of the Snowy Range in the state of Wyoming, a portion of the Rocky Mountains. Acetone ($\geq 99.5\%$, high-performance liquid chromatography [HPLC]), potassium hydroxide (KOH) ($\geq 85.0\%$ KOH basis), N,N-dimethylformamide (DMF) ($\geq 99.9\%$, HPLC), and PAN (average Mw 150,000 g mol⁻¹) were purchased from Sigma-Aldrich. Ultra-zero grade air (total

hydrocarbons <0.1 ppm) and ultra-high purity grade nitrogen gas (N₂) (99.999%) were purchased from United States Welding. All materials were used as received.

Preparation of CNFs Precursors

Prior to all tests, the raw pinewood was chopped and milled into particles with an average size of 0.5 mm and dried overnight at 120°C. Pyrolysis degradation of pinewood particles was conducted in a quartz glass reactor heated by a solar simulator manufactured by a calibrated high-power xenon bulb as an energy source instead of the real sun to produce SDBL shown in Figure S6. About 2 g pinewood particles were loaded into a cylindrical, quartz glass reactor with an inner diameter of 29 mm. The solar flux was kept constant at 355 suns (the temperature is 750°C). Then, the reactor was placed at the focus of the solar simulator for 30 min.

Also, TDBL was generated by using a thermal pyrolysis setup shown in Figure S7. The furnace (Lindberg/Blue M tube furnace, Thermo Scientific) was heated to 750°C. About 2 g pinewood particles were loaded into the constant temperature area of the quartz tube reactor (inner diameter: 10 mm) and purged with 100 mL/min N₂. Then, the reactor was put into a furnace for 30 min.

Salt (anhydrous sodium sulfate) and bioliquids were blended in the ratio of 1:1 to make the bioliquid-water mixture in a sealed container, followed by putting the mixture in an ultrasonic bath for 20 min at room temperature, filtering out the mixture for removal of the salt and other solids, and collecting the oil (with acetone). The acetone in the oil was removed under the pressure of 556 mbar at a temperature of 60°C. The dewatered SDBL and TDBL were abbreviated as DWSDBL and DWTDBL, respectively.

Synthesis of Supercapacitor Electrodes

In this research, the mixtures of DWSDBL or DWTDBL and 7.8 wt % PAN solutions were used for synthesizing fresh CNFs. 7.8 wt % PAN solution was prepared by dissolving PAN into DMF. The ratios of DWSDBL or DWTDBL to PAN in the DWSDBL-PAN or DWTDBL-PAN mixtures used for electrospinning are listed in Table S7. The custom-made electrospinning setup was made up of three parts: a high-voltage power supply (Gamma High Voltage, ES30P-5W); a single syringe pump (Fisher Scientific); and a collector (Figure S8). Electrospinning was performed under the operation voltage of 15 kV with a distance of 15 cm between needle tip and collector at the flow rate of 0.6 mL h⁻¹. The obtained fresh nanofibers were placed into a ceramic crucible boat. Those samples were stabilized by heating from 25°C to 300°C with a ramping rate of 1°C min⁻¹ under an airflow of 100 mL min⁻¹ and holding for 3 h in a Lindberg/Blue M tube furnace (Thermo Scientific). Then, the stabilized samples were carbonized at 800°C at a heating rate of 10°C min⁻¹ for 1 h with a 100 mL min⁻¹ N₂ flow.

Electrochemical Performance Evaluation

The electrochemical properties of the finished CNFs were evaluated with an electrochemical workstation (CHI 6203D, CH Instruments, Japan). 6 M KOH solution was used as an electrolyte, while Hg/HgO electrode and a 5 cm² platinum foil as well as a 1.0 × 1.0 cm CNFs with pressed nickel foams on both sides were employed as the reference electrode, counter electrode, and working electrode, respectively. The mass loading of the active electrodes is ~1.5 mg cm⁻². CVs of the DWSDBL-PAN- or DWTDBL-PAN-derived supercapacitor electrodes were obtained with a potential window of -0.9 to 0 V versus Hg/HgO at scan rates of 5–100 mV s⁻¹. Also, the GCD characteristics of the supercapacitor electrodes were observed under the

current densities 0.5–20 A g⁻¹. Their EISs were measured within the frequency range of 10,000–0.01 Hz. The specific capacities (C_s) of the supercapacitor electrodes were calculated using GCD curves via the following equation:³⁹

$$C_s \text{ (F g}^{-1}\text{)} = \frac{I \times \Delta t}{m \times \Delta V} \quad \text{(Equation 3)}$$

where C_s is the specific capacitances (F g⁻¹); I is the discharge current (A); V is the potential window (V); and m is the loading mass (g).

The setup used for evaluating the electrochemical performance of DWSDBL30PAN70 CNFs or supercapacitor electrodes is given in Figure S9. The specific capacity (C_t) of the single electrode and the specific capacitance (C_{sp}) of the supercapacitor cell were calculated using GCD curves Equations 4 and 5, respectively. The energy density (E) was calculated using Equation 6, although power density was calculated with Equation 7.⁴⁰

$$C_t \text{ (F g}^{-1}\text{)} = \frac{2 \times I \times \Delta t}{m \times \Delta V}, \quad \text{(Equation 4)}$$

$$C_{sp} \text{ (F g}^{-1}\text{)} = 4 \times C_t, \quad \text{(Equation 5)}$$

$$E \text{ (Wh Kg}^{-1}\text{)} = \frac{C_s V^2 \times 3.6}{2}, \quad \text{(Equation 6)}$$

$$P \text{ (W Kg}^{-1}\text{)} = \frac{E \times 3600}{\Delta t d}, \quad \text{(Equation 7)}$$

where C_t is the specific capacitance (F g⁻¹) of a single electrode, m represents the loading mass (g) of a single electrode, C_{sp} denotes the specific capacitance (F g⁻¹) of the supercapacitor cell, ΔV is the potential window (V), I is the discharge current (A), and td is the discharge time (s).

Materials Characterization

The proximate and ultimate analyses of pinewood were determined by ASTM D5142-02, and the results are provided in Table S8. FTIR spectroscopy (Nicolet iS50, Thermo Scientific) with non-destructive attenuated total reflectance technique and Agilent Technology 7890B/5977B GC-MS system was used to characterize the chemical properties of bioliquid prepared from the solar pyrolysis system. A TGA (SDT-Q600, TA instrument) was applied to quantitatively determine the mass loss characteristics of bioliquids and the final carbon yield of the prepared CNFs. The morphology of the fibers was studied by using a SEM (Quanta 250, FEI), an AFM (Asylum Research MFP-3D, Oxford), and a high-resolution transmission electron microscopy (HR-TEM) (JEM-2100, JEOL). The specific surface area and pore size distribution of the prepared samples were measured with a BET (Quantachrome, Autosorb-iQ system) analyzer. XRD (Smartlab diffraction system, Rigaku) measurement and Raman (Sierra IM-52, Snowy Range Instruments) were conducted to verify the phase expression and the presence of graphitic carbon. XPS (5800, Physical Electronics') was performed with a monochromatic AlKα as an X-ray source. The binding energy scales were calibrated with C1s peak at 284.8 eV being the reference.

SUPPLEMENTAL INFORMATION

Supplemental Information can be found online at <https://doi.org/10.1016/j.xcrp.2020.100079>.

ACKNOWLEDGMENTS

The authors thank the National Science Foundation of United States (NSF OIA-1632899, NSF 1632899, and NSF 1430001) for their support for this research.

AUTHOR CONTRIBUTIONS

T.W. and K.S. processed the experimental data, performed the analysis, and drafted the manuscript. A.H.R. and W.L. prepared the bioliquids using solar and thermal pyrolysis. W.G., X.H., and M.T. manufactured the samples and characterized them with GC-MS, FTIR, and TGA. J.Y. and H.L. aided in interpreting the results of the electrochemical performance and worked on the manuscript. L.K. and S.J.S. performed the test of AFM and TEM. R.Y. manufactured the samples and characterized them with XPS. E.G.E. and M.F. supervised the project.

DECLARATION OF INTERESTS

The authors declare no competing interests.

Received: February 18, 2020

Revised: April 18, 2020

Accepted: May 7, 2020

Published: June 24, 2020

REFERENCES

- Kannan, N., and Vakeesan, D. (2016). Solar energy for future world: - a review. *Renew. Sustain. Energy Rev.* 62, 1092–1105.
- Enevoldsen, P., and Sovacool, B.K. (2016). Examining the social acceptance of wind energy: practical guidelines for onshore wind project development in France. *Renew. Sustain. Energy Rev.* 53, 178–184.
- Moya, D., Aldás, C., and Kaparaju, P. (2018). Geothermal energy: power plant technology and direct heat applications. *Renew. Sustain. Energy Rev.* 94, 889–901.
- Lu, H., and Zhao, X.S. (2017). Biomass-derived carbon electrode materials for supercapacitors. *Sustainable Energy Fuels* 1, 1265–1281.
- Pathak, R., Chen, K., Gurung, A., Reza, K.M., Bahrami, B., Pokharel, J., Baniya, A., He, W., Wu, F., Zhou, Y., et al. (2020). Fluorinated hybrid solid-electrolyte-interphase for dendrite-free lithium deposition. *Nat. Commun.* 11, 93.
- Chen, K., Pathak, R., Gurung, A., Reza, K.M., Ghimire, N., Pokharel, J., Baniya, A., He, W., Wu, J.J., Qiao, Q.Q., et al. (2020). A copper-clad lithiophilic current collector for dendrite-free lithium metal anodes. *J. Mater. Chem. A* 8, 1911–1919.
- Gurung, A., Chen, K., Khan, R., Abdulkarim, S.S., Varnekar, G., Pathak, R., Naderi, R., and Qiao, Q. (2017). Highly efficient perovskite solar cell photocharging of lithium ion battery using DC–DC booster. *Adv. Energy Mater.* 7, 1602105.
- Chen, K., Pathak, R., Gurung, A., Adhamash, E.A., Bahrami, B., He, Q., Qiao, H., Smirnova, A.L., Wu, J.J., Qiao, Q., et al. (2019). Flower-shaped lithium nitride as a protective layer via facile plasma activation for stable lithium metal anodes. *Energy Storage Materials* 18, 389–396.
- Pathak, R., Chen, K., Gurung, A., Reza, K.M., Bahrami, B., Wu, F., Chaudhary, A., Ghimire, N., Zhou, B., Zhang, W.-H., et al. (2019). Ultrathin bilayer of graphite/SiO₂ as solid interface for reviving Li metal anode. *Adv. Energy Mater.* 9, 1901486.
- Jin, H., Li, J., Yuan, Y., Wang, J., Lu, J., and Wang, S. (2018). Recent progress in biomass-derived electrode materials for high volumetric performance supercapacitors. *Adv. Energy Mater.* 8, 1801007.
- Lu, S.-Y., Jin, M., Zhang, Y., Niu, Y.-B., Gao, J.-C., and Li, C.M. (2018). Chemically exfoliating biomass into a graphene-like porous active carbon with rational pore structure, good conductivity, and large surface area for high-performance supercapacitors. *Adv. Energy Mater.* 8, 1702545.
- Li, B., Dai, F., Xiao, Q., Yang, L., Shen, J., Zhang, C., and Cai, M. (2016). Nitrogen-doped activated carbon for a high energy hybrid supercapacitor. *Energy Environ. Sci.* 9, 102–106.
- Yu, L., Hu, L., Anasori, B., Liu, Y.-T., Zhu, Q., Zhang, P., Gogotsi, Y., and Xu, B. (2018). MXene-bonded activated carbon as a flexible electrode for high-performance supercapacitors. *ACS Energy Lett.* 3, 1597–1603.
- Ma, F., Ding, S., Ren, H., and Liu, Y. (2019). Sakura-based activated carbon preparation and its performance in supercapacitor applications. *RSC Advances* 9, 2474–2483.
- Ma, Y., Chang, H., Zhang, M., and Chen, Y. (2015). Graphene-based materials for lithium-ion hybrid supercapacitors. *Adv. Mater.* 27, 5296–5308.
- Li, P., Jin, Z., Peng, L., Zhao, F., Xiao, D., Jin, Y., and Yu, G. (2018). Stretchable all-gel-state fiber-shaped supercapacitors enabled by macromolecularly interconnected 3D graphene/nanostructured conductive polymer hydrogels. *Adv. Mater.* 30, e1800124.
- Zhang, L., Chen, Z., Zheng, S., Qin, S., Wang, J., Chen, C., Liu, D., Wang, L., Yang, G., Su, Y., et al. (2019). Shape-tailorable high-energy asymmetric micro-supercapacitors based on plasma reduced and nitrogen-doped graphene oxide and MoO₂ nanoparticles. *J. Mater. Chem. A* 7, 14328–14336.
- Yu, S., Yang, N., Vogel, M., Mandal, S., Williams, O.A., Jiang, S., Schönherr, H., Yang, B., and Jiang, X. (2018). Battery-like supercapacitors from vertically aligned carbon nanofiber coated diamond: design and demonstrator. *Adv. Energy Mater.* 8, 1702947.
- Zhang, H., Xie, Z., Wang, Y., Shang, X., Nie, P., and Liu, J. (2017). Electrospun polyacrylonitrile/ β -cyclodextrin based porous carbon nanofiber self-supporting electrode for capacitive deionization. *RSC Advances* 7, 55224–55231.
- Zhang, L.L., and Zhao, X.S. (2009). Carbon-based materials as supercapacitor electrodes. *Chem. Soc. Rev.* 38, 2520–2531.
- Pan, H., Li, J., and Feng, Y. (2010). Carbon nanotubes for supercapacitor. *Nanoscale Res. Lett.* 5, 654–668.
- Khairnar, V., Sharon, M., Jaybhaye, S., and Neumann, M. (2006). Development of supercapacitor using carbon nanofibers synthesized from ethanol. *Synth. React. Inorg. Met.-Org. Nano-Met. Chem.* 36, 171–173.

23. Wang, Y., Shi, Z., Huang, Y., Ma, Y., Wang, C., Chen, M., and Chen, Y. (2009). Supercapacitor devices based on graphene materials. *J. Phys. Chem. C* 113, 13103–13107.
24. Barranco, V., Lillo-Rodenas, M.A., Linares-Solano, A., Oya, A., Pico, F., Ibañez, J., Agullo-Rueda, F., Amarilla, J.M., and Rojo, J.M. (2010). Amorphous carbon nanofibers and their activated carbon nanofibers as supercapacitor electrodes. *J. Phys. Chem. C* 114, 10302–10307.
25. Manawi, Y.M., Ihsanulla, Samara, A., Al-Ansari, T., and Atieh, M.A. (2018). A review of carbon nanomaterials' synthesis via the chemical vapor deposition (CVD) method. *Materials (Basel)* 11, 822.
26. Inagaki, M., Yang, Y., and Kang, F. (2012). Carbon nanofibers prepared via electrospinning. *Adv. Mater.* 24, 2547–2566.
27. Gurung, A., Pokharel, J., Baniya, A., Pathak, R., Chen, K., Lamsal, B.S., Ghimire, N., Zhang, W.-H., Zhou, Y., and Qiao, Q. (2019). A review on strategies addressing interface incompatibilities in inorganic all-solid-state lithium batteries. *Sustainable Energy Fuels* 3, 3279–3309.
28. Jirsak, O., Sysel, P., Sanetrik, F., Hruza, J., and Chaloupek, J. (2010). Polyamic acid nanofibers produced by needlessly electrospinning. *J. Nanomater.* 2010, 842831.
29. Liu, Y., and Guo, L. (2013). Homogeneous field intensity control during multi-needle electrospinning via finite element analysis and simulation. *J. Nanosci. Nanotech.* 13, 843–847.
30. Peng, H., Wang, D., and Fu, S. (2020). Tannic acid-assisted green exfoliation and functionalization of MoS₂ nanosheets: significantly improve the mechanical and flame-retardant properties of polyacrylonitrile composite fibers. *Chem. Eng. J.* 384, 123288.
31. Xue, T.J., McKinney, M.A., and Wilkie, C.A. (1997). The thermal degradation of polyacrylonitrile. *Polym. Degrad. Stabil.* 58, 193–202.
32. Nielsen, M., Jurasek, P., Hayashi, J., and Furimsky, E. (1995). Formation of toxic gases during pyrolysis of polyacrylonitrile and nylons. *J. Anal. Appl. Pyrolysis* 35, 43–51.
33. Szepecsik, B., and Pukánszky, B. (2019). The mechanism of thermal stabilization of polyacrylonitrile. *Thermochim. Acta* 671, 200–208.
34. Liu, W.-J., Tian, K., He, Y.-R., Jiang, H., and Yu, H.-Q. (2014). High-yield harvest of nanofibers/mesoporous carbon composite by pyrolysis of waste biomass and its application for high durability electrochemical energy storage. *Environ. Sci. Technol.* 48, 13951–13959.
35. Guedes, R.E., Luna, A.S., and Torres, A.R. (2018). Operating parameters for bio-oil production in biomass pyrolysis: A review. *J. Anal. Appl. Pyrolysis* 129, 134–149.
36. Nzihou, A., Flamant, G., and Stanmore, B. (2012). Synthetic fuels from biomass using concentrated solar energy – A review. *Energy* 42, 121–131.
37. Rony, A.H., Mosiman, D., Sun, Z., Qin, D., Zheng, Y., Boman, J.H., IV, and Fan, M. (2018). A novel solar powered biomass pyrolysis reactor for producing fuels and chemicals. *J. Anal. Appl. Pyrolysis* 132, 19–32.
38. Lu, L.-L., Lu, Y.-Y., Xiao, Z.-J., Zhang, T.-W., Zhou, F., Ma, T., Ni, Y., Yao, H.-B., Yu, S.-H., and Cui, Y. (2018). Wood-inspired high-performance ultrathick bulk battery electrodes. *Adv. Mater.* 30, e1706745.
39. Manyala, N., Bello, A., Barzegar, F., Khaleed, A.A., Momodu, D.Y., and Dangbegnon, J.K. (2016). Coniferous pine biomass: a novel insight into sustainable carbon materials for supercapacitors electrode. *Mater. Chem. Phys.* 182, 139–147.
40. Karthikeyan, K., Amaresh, S., Lee, S.N., Sun, X., Aravindan, V., Lee, Y.-G., and Lee, Y.S. (2014). Construction of high-energy-density supercapacitors from pine-cone-derived high-surface-area carbons. *ChemSusChem* 7, 1435–1442.
41. Kędzierska-Matyszek, M., Matwijczuk, A., Florek, M., Barłowska, J., Wolanczuk, A., Matwijczuk, A., Chruściel, E., Walkowiak, R., Karcz, D., and Gladyszewska, B. (2018). Application of FTIR spectroscopy for analysis of the quality of honey. *BIO Web Conf.* 10, 02008.
42. Majeed, M.I., Guo, J., Yan, W., and Tan, B. (2016). Preparation of magnetic iron oxide nanoparticles (MIONs) with improved saturation magnetization using multifunctional polymer ligand. *Polymers (Basel)* 8, E392.
43. Lv, Y., Gan, L., Liu, M., Xiong, W., Xu, Z., Zhu, D., and Wright, D.S. (2012). A self-template synthesis of hierarchical porous carbon foams based on banana peel for supercapacitor electrodes. *J. Power Sources* 209, 152–157.
44. Böcker, U., Wubshet, S.G., Lindberg, D., and Afseth, N.K. (2017). Fourier-transform infrared spectroscopy for characterization of protein chain reductions in enzymatic reactions. *Analyst (Lond.)* 142, 2812–2818.
45. Zhang, P., Guo, Y.-J., Chen, J., Zhao, Y.-R., Chang, J., Junge, H., Beller, M., and Li, Y. (2018). Streamlined hydrogen production from biomass. *Nat. Catal.* 1, 332–338.
46. Yang, T., Qian, T., Wang, M., Shen, X., Xu, N., Sun, Z., and Yan, C. (2016). A sustainable route from biomass byproduct Okara to high content nitrogen-doped carbon sheets for efficient sodium ion batteries. *Adv. Mater.* 28, 539–545.
47. Borghei, M., Lehtonen, J., Liu, L., and Rojas, O.J. (2018). Advanced biomass-derived electrocatalysts for the oxygen reduction reaction. *Adv. Mater.* 30, e1703691.
48. Zhao, C., and Lercher, J.A. (2012). Upgrading pyrolysis oil over Ni/HZSM-5 by cascade reactions. *Angew. Chem. Int. Ed. Engl.* 51, 5935–5940.
49. Ferrini, P., and Rinaldi, R. (2014). Catalytic biorefining of plant biomass to non-pyrolytic lignin bio-oil and carbohydrates through hydrogen transfer reactions. *Angew. Chem. Int. Ed. Engl.* 53, 8634–8639.
50. Wu, M., Wang, Q., Li, K., Wu, Y., and Liu, H. (2012). Optimization of stabilization conditions for electrospun polyacrylonitrile nanofibers. *Polym. Degrad. Stabil.* 97, 1511–1519.
51. Zhou, Z., Lai, C., Zhang, L., Qian, Y., Hou, H., Reneker, D.H., and Fong, H. (2009). Development of carbon nanofibers from aligned electrospun polyacrylonitrile nanofiber bundles and characterization of their microstructural, electrical, and mechanical properties. *Polymer* 50, 2999–3006.
52. Goudarzi, A., Lin, L.-T., and Ko, F.K. (2014). X-Ray diffraction analysis of Kraft lignins and lignin-derived carbon nanofibers. *J. Nanotechnol. Eng. Med.* 5, 021006.
53. Kim, C., Park, S.-H., Cho, J.-I., Lee, D.-Y., Park, T.-J., Lee, W.-J., and Yang, K.-S. (2004). Raman spectroscopic evaluation of polyacrylonitrile-based carbon nanofibers prepared by electrospinning. *J. Raman Spectrosc.* 35, 928–933.
54. Shan, D., Yang, J., Liu, W., Yan, J., and Fan, Z. (2016). Biomass-derived three-dimensional honeycomb-like hierarchical structured carbon for ultrahigh energy density asymmetric supercapacitors. *J. Mater. Chem. A* 4, 13589–13602.
55. Gong, Y., Li, D., Luo, C., Fu, Q., and Pan, C. (2017). Highly porous graphitic biomass carbon as advanced electrode materials for supercapacitors. *Green Chem.* 19, 4132–4140.
56. Yang, C.-H., Nguyen, Q.D., Chen, T.-H., Helal, A.S., Li, J., and Chang, J.-K. (2018). Functional group-dependent supercapacitive and aging properties of activated carbon electrodes in organic electrolyte. *ACS Sustain. Chem. Eng.* 6, 1208–1214.
57. Oh, Y.J., Yoo, J.J., Kim, Y.I., Yoon, J.K., Yoon, H.N., Kim, J.-H., and Park, S.B. (2014). Oxygen functional groups and electrochemical capacitive behavior of incompletely reduced graphene oxides as a thin-film electrode of supercapacitor. *Electrochim. Acta* 116, 118–128.
58. Yu, M., Xie, B., Yang, Y., Zhang, Y., Chen, Y., Yu, W., Zhang, S., Lu, L., and Liu, D. (2017). Residual oxygen groups in nitrogen-doped graphene to enhance the capacitive performance. *RSC Advances* 7, 15293–15301.
59. He, Y., Zhang, Y., Li, X., Lv, Z., Wang, X., Liu, Z., and Huang, X. (2018). Capacitive mechanism of oxygen functional groups on carbon surface in supercapacitors. *Electrochim. Acta* 282, 618–625.
60. Baek, G.Y., Lee, H.S., Jung, J.-M., Hwang, I.-T., Shin, J., Jung, C.-H., and Choi, J.-H. (2018). Preparation of conductive carbon films from polyacrylonitrile/graphene oxide composite films by thermal treatment. *J. Ind. Eng. Chem.* 58, 87–91.
61. Zhang, L., Wang, X., Wang, R., and Hong, M. (2015). Structural evolution from metal-organic framework to hybrids of nitrogen-doped porous carbon and carbon nanotubes for enhanced oxygen reduction activity. *Chem. Mater.* 27, 7610–7618.
62. Wang, M., Hu, B., Ji, H., Song, Y., Liu, J., Peng, D., He, L., and Zhang, Z. (2017). Aptasensor based on hierarchical core-shell nanocomposites of zirconium hexacyanoferrate nanoparticles and mesoporous mFe₃O₄@mC: electrochemical quantitation of epithelial tumor marker mucin-1. *ACS Omega* 2, 6809–6818.
63. Tan, S., Kraus, T.J., and Li-Oakey, K.D. (2019). Understanding the supercapacitor properties

- of electrospun carbon nanofibers from Powder River Basin coal. *Fuel* 245, 148–159.
64. Xu, C., Xu, B., Gu, Y., Xiong, Z., Sun, J., and Zhao, X.S. (2013). Graphene-based electrodes for electrochemical energy storage. *Energy Environ. Sci.* 6, 1388–1414.
 65. Cheng, Y., Huang, L., Xiao, X., Yao, B., Yuan, L., Li, T., Hu, Z., Wang, B., Wan, J., and Zhou, J. (2015). Flexible and cross-linked N-doped carbon nanofiber network for high performance freestanding supercapacitor electrode. *Nano Energy* 15, 66–74.
 66. Tan, Y., Lin, D., Liu, C., Wang, W., Kang, L., and Ran, F. (2018). Carbon nanofibers prepared by electrospinning accompanied with phase-separation method for supercapacitors: effect of thermal treatment temperature. *J. Mater. Res.* 33, 1120–1130.
 67. Li, P., Yang, Y., Shi, E., Shen, Q., Shang, Y., Wu, S., Wei, J., Wang, K., Zhu, H., Yuan, Q., et al. (2014). Core-double-shell, carbon nanotube@polypyrrole@MnO₂ sponge as freestanding, compressible supercapacitor electrode. *ACS Appl. Mater. Interfaces* 6, 5228–5234.
 68. Pathak, R., Gurung, A., Elbohy, H., Chen, K., Reza, K.M., Bahrami, B., Mabrouk, S., Ghimire, R., Hummel, M., Gu, Z., et al. (2018). Self-recovery in Li-metal hybrid lithium-ion batteries via WO₃ reduction. *Nanoscale* 10, 15956–15966.
 69. Guo, M., Guo, J., Jia, D., Zhao, H., Sun, Z., Song, X., and Li, Y. (2015). Coal derived porous carbon fibers with tunable internal channels for flexible electrodes and organic matter absorption. *J. Mater. Chem. A* 3, 21178–21184.
 70. Gao, L., Surjadi, J.U., Cao, K., Zhang, H., Li, P., Xu, S., Jiang, C., Song, J., Sun, D., and Lu, Y. (2017). Flexible fiber-shaped supercapacitor based on nickel-cobalt double hydroxide and pen ink electrodes on metallized carbon fiber. *ACS Appl. Mater. Interfaces* 9, 5409–5418.
 71. Cakici, M., Kakarla, R.R., and Alonso-Marroquin, F. (2017). Advanced electrochemical energy storage supercapacitors based on the flexible carbon fiber fabric-coated with uniform coral-like MnO₂ structured electrodes. *Chem. Eng. J.* 309, 151–158.
 72. Abioye, A.M., and Ani, F.N. (2015). Recent development in the production of activated carbon electrodes from agricultural waste biomass for supercapacitors: a review. *Renew. Sustain. Energy Rev.* 52, 1282–1293.
 73. Ma, C., Cao, E., Li, J., Fan, Q., Wu, L., Song, Y., and Shi, J. (2018). Synthesis of mesoporous ribbon-shaped graphitic carbon nanofibers with superior performance as efficient supercapacitor electrodes. *Electrochim. Acta* 292, 364–373.